

## NON-EQUILIBRIUM IONIZATION MODELING OF THE CURRENT SHEET IN A SIMULATED SOLAR ERUPTION

CHENGCAI SHEN<sup>1,2,3</sup>, KATHARINE K. REEVES<sup>1</sup>, JOHN C. RAYMOND<sup>1</sup>, NICHOLAS A. MURPHY<sup>1</sup>,  
YUAN-KUEN KO<sup>4</sup>, JUN LIN<sup>2</sup>, ZORAN MIKIĆ<sup>5</sup>, AND JON A. LINKER<sup>5</sup>

<sup>1</sup> Harvard-Smithsonian Center for Astrophysics, 60 Garden Street, Cambridge, MA 02138, USA

<sup>2</sup> Yunnan Astronomical Observatory, Chinese Academy of Sciences, P. O. Box 110, Kunming, Yunnan 650011, China

<sup>3</sup> Graduate School of the Chinese Academy of Sciences, Beijing 100039, China

<sup>4</sup> Space Science Division, Naval Research Laboratory, Washington, DC 20375, USA

<sup>5</sup> Predictive Science, Inc. (PSI), San Diego, CA 92121-2910, USA

Received 2013 March 13; accepted 2013 May 18; published 2013 July 31

### ABSTRACT

The current sheet that extends from the top of flare loops and connects to an associated flux rope is a common structure in models of coronal mass ejections (CMEs). To understand the observational properties of CME current sheets, we generated predictions from a flare/CME model to be compared with observations. We use a simulation of a large-scale CME current sheet previously reported by Reeves et al. This simulation includes ohmic and coronal heating, thermal conduction, and radiative cooling in the energy equation. Using the results of this simulation, we perform time-dependent ionization calculations of the flow in a CME current sheet and construct two-dimensional spatial distributions of ionic charge states for multiple chemical elements. We use the filter responses from the Atmospheric Imaging Assembly (AIA) on the *Solar Dynamics Observatory* and the predicted intensities of emission lines to compute the count rates for each of the AIA bands. The results show differences in the emission line intensities between equilibrium and non-equilibrium ionization. The current sheet plasma is underionized at low heights and overionized at large heights. At low heights in the current sheet, the intensities of the AIA 94 Å and 131 Å channels are lower for non-equilibrium ionization than for equilibrium ionization. At large heights, these intensities are higher for non-equilibrium ionization than for equilibrium ionization inside the current sheet. The assumption of ionization equilibrium would lead to a significant underestimate of the temperature low in the current sheet and overestimate at larger heights. We also calculate the intensities of ultraviolet lines and predict emission features to be compared with events from the Ultraviolet Coronagraph Spectrometer on the *Solar and Heliospheric Observatory*, including a low-intensity region around the current sheet corresponding to this model.

*Key words:* atomic processes – magnetic reconnection – Sun: coronal mass ejections (CMEs) – Sun: UV radiation

*Online-only material:* color figures

### 1. INTRODUCTION

The coronal mass ejection (CME)/flare current sheet is a large-scale structure that connects the flare to the associated CME during a solar eruption. In the classic two-ribbon flare model, for instance, the well-known CSHKP model (e.g., Carmichael 1964; Sturrock 1968; Hirayama 1974; Kopp & Pneuman 1976), magnetic reconnection occurs rapidly inside the current sheet above the flare, and the magnetic energy is converted into the heat and kinetic energy of the plasma, as well as the kinetic energy of energetic particles. Martens & Kuin (1989) and Lin & Forbes (2000) extended this framework into the catastrophe model of solar eruptions, in which the current sheet forms dynamically and evolves into a long and thin structure as the CME propagates into interplanetary space. In this case, the current sheet top could extend out beyond 10 solar radii with the CME (e.g., see Web et al. 2003), and the bottom end is near the top of the X-ray flare loops. However, many CME current sheets are, in fact, not as radially extended (e.g., see Ko et al. 2003), and the location of the current sheet may change in an event (e.g., see Lin et al. 2005, their Figure 4). The lifetime of CME current sheets differs from event to event and also depends on the wavelength observed. For instance, the current sheet observed on [Fe XVIII] lasts several hours (Ciaravella & Raymond 2008), and other observations demonstrated the [Fe XVIII] emission may last for even two days (Ko et al. 2003; Bemporad

et al. 2006). In observations of white light images, some studies reveal that current sheets may persist for more than 10 hr (Ko et al. 2003; Lin et al. 2005; Ciaravella et al. 2013). However, some events are relatively short, lasting only a few minutes (e.g., see Raymond et al. 2003). Magnetic reconnection occurring inside the current sheet creates upward and downward outflows from the X-point and causes the flare loops to grow in the low corona. The release of magnetic tension over the flux rope by reconnection causes the CMEs to propagate away from the Sun.

Related to the above theoretical works, a series of observations provided evidence for the formation and development of the CME/flare current sheet (e.g., see Ciaravella et al. 2002; Ko et al. 2003; Raymond et al. 2003; Web et al. 2003; Lin et al. 2005; Bemporad et al. 2006; Ciaravella & Raymond 2008; Reeves & Golub 2011; Savage et al. 2010; Landi et al. 2010, 2012). The fundamental properties of these current sheets have been studied using spectral diagnostics (see also Kohl et al. 2006). Among the topics studied, time-dependent ionization is very important. In the observed current sheets, the ionization timescale of some ions is longer than the dynamical timescale associated with the high-speed reconnection outflow. For example, the ionization timescale of Fe XVIII is about  $10^3$  s in the coronal environment at several solar radii, while the flow timescale is several times smaller for characteristic reconnection outflow velocities of  $10^3$  km s<sup>-1</sup>. This implies that the plasma inside the current sheet may not be in ionization equilibrium.

Time-dependent ionization processes have been investigated in several previous studies of flares and CMEs (e.g., Rakowski et al. 2007, 2011; Gruesbeck et al. 2011, 2012; Lynch et al. 2011; Reinard et al. 2012; Akmal et al. 2001; Murphy et al. 2011). Rakowski et al. (2007) studied the charge state distributions of the ions of various elements in interplanetary CMEs (ICMEs). By integrating the time-dependent ionization equation for a model of CME evolution and comparing with in situ data from the *Advanced Composition Explorer* (*ACE*), they found that extra heating is required to explain the CME “core.” Lynch et al. (2011) studied the ionic charge state composition using two different asymmetric MHD simulations of CME, including the one we are using in this work and one using a breakout-type configuration. They integrated the time-dependent ionization equation according to the evolution history of the temperature and electron density from the simulation results, and constructed two-dimensional (2D) distributions of commonly measured ionic charge state ratios of several elements that are typically elevated in ICMEs. They found that the CME with an extended current sheet has elevated charge states in the ICMEs, while the other simulated CME with a relatively short current sheet length and duration has no charge state enhancement in the flux rope. By analyzing *ACE* and *Solar Terrestrial Relations Observatory* data as well as MHD simulation results, Reinard et al. (2012) reported that the flux rope center is relatively cool, while charge state enhancements surround and trail the flux ropes. This is consistent with the predictions by Lin et al. (2004) and Lin & Soon (2004).

In studies of the reconnecting current sheet, several authors reported calculations of time-dependent ionization. Ko et al. (2010) modeled UV and X-ray emissions by considering the time-dependent ionization in a steady-state Petschek-type reconnection scheme for the post-CME current sheet. They found that the predicted emission intensities are consistent with *Solar and Heliospheric Observatory* (*SOHO*)/Ultraviolet Coronagraph Spectrometer (UVCS) and *Hinode*/X-ray Telescope observations of post-CME current sheets. Using three combinations of temperature and density profiles, they investigated the effect of coronal parameters and suggested that the coronal electron density profile is the most important factor in determining the emission properties inside the current sheet. Imada et al. (2011) reported the effects of time-dependent ionization and recombination in magnetic reconnection in the solar corona. They calculated the ionization charge states of iron in Petschek-type reconnection structures, and noticed that the iron is mostly in non-equilibrium ionization in the reconnection region.

In this work, we focus on the time-dependent ionization inside a large-scale and dynamically developed CME/flare current sheet. As compared to previous studies (Ko et al. 2010), we deal with the CME/flare current sheet formed in the full CME/flare eruption model of Reeves et al. (2010). In this case, the simulations provide the full history of the current sheet evolution, including detailed distribution of temperature and electron density. The same CME/flare eruption model is used by Lynch et al. (2011), but they focused on the charge states of several heavy elements in the flux rope itself. To complement their research, we look at the ionization processes in the CME/flare current sheet regions, in which the high-temperature plasma outflows are result of magnetic reconnection occurring in the larger scale sheet. The corresponding ionization properties inside the current sheet are quite different from those in the flux rope.

Reeves et al. (2010) constructed a CME model using a 2.5D numerical MHD simulation that includes ohmic dissipation, coronal heating, thermal conduction, and radiative cooling in the energy equation. The simulation domain extends from 1 to 20 solar radii. The simulation showed the development of a thin current sheet that extends under the flux rope as the CME moves upward. Using the temperature and density from this simulation, they calculated the X-ray and the extreme-ultraviolet (EUV) emissions from the flare loops and predicted the structures surrounding the current sheet, assuming ionization equilibrium (e.g., see also Reeves & Golub 2011, for predicted Atmospheric Imaging Assembly (AIA) emission). The predicted X-ray images of the current sheet indicate that the current sheet should be visible in soft X-rays.

Using the simulation data provided by Reeves et al. (2010), we predict the observational characteristics of the current sheet and discuss where the time-dependent ionization is important and the assumption of equilibrium ionization could be misleading. In Section 2, we introduce the methods to solve the time-dependent ionization equation, and the process of calculating emission intensities for *Solar Dynamics Observatory* (*SDO*)/AIA bands. In the next section, we show the calculation results. First, we give the ion charge states of several elements that are important to observations of CME/flare current sheets, and study the features of ion charge states in the region around the current sheet. Then we study the properties of predicted count rates of *SDO*/AIA bands and the predicted intensities of UV (and EUV) emission lines corresponding to *SOHO*/UVCS observations.

## 2. METHODS

From the 2.5D MHD numerical simulation of Reeves et al. (2010), the evolution of the CME/flare with time and the distributions of temperature ( $T$ ) and plasma density ( $\rho$ ) around the CME/flare current sheet at any time are known on the 2D plane. To get properties of emission lines along the line of sight (LOS), we assume that the coronal plasma is optically thin in the analysis below. Therefore the local electron density, temperature, length along the LOS, and the ionization states predict the emission line intensity. To get ion charge states from the simulation, we need to solve the time-dependent ionization equations.

First, we find the evolutionary history of temperature and electron density for any position near the current sheet at a given simulation time below the erupting CME flux rope. In local regions including the current sheet, we define a group of cells on the mesh grids of numerical calculations, and then trace the motion of each cell back to an early time in the CME/flare system evolution. We trace the trajectory of any cell according to the time-dependent velocity field from MHD simulation data. Using a predictor–corrector method, we solve the motion equation and integrate the velocities backward in time to get the plasma trajectories. In this way, for any given initial time and position for a cell, a “streamline” is plotted in a Lagrangian framework, so the motion history is clear. For each streamline, it is easy to get the evolution of  $T$  and  $\rho$  with time by using bilinear interpolation in space and spline interpolation in time.

Since this CME/flare model includes a spherically symmetric solar wind solution in the beginning, which forms a helmet streamer in the later time, most of the plasma is predicted to move up from the solar surface. In this case, the initial location of each moving cell should be the surface of the Sun, and those “streamlines” root at the solar surface. These simulations also include a dense, cool chromosphere and a transition region.

We define a critical height  $r = 1.02R_\odot$  and calculate time-dependent ionization processes if the plasma moves up and crosses this critical height. Below this critical height, the electron density is so high (e.g.,  $>10^9 \text{ cm}^{-3}$ ) that ionization timescales are very short and plasma can be considered to be in ionization equilibrium.

The charge state evolution for a moving parcel of plasma is given by

$$\frac{df_i}{dt} = n_e(C_{i-1}f_{i-1} - (C_i + R_i)f_i + R_{i+1}f_{i+1}), \quad (1)$$

where  $f_i$  is ionic fraction,  $n_e$  is electron density, and  $C_i$  and  $R_i$  are the ionization rate and recombination rates for this ion, respectively. The ionization rate includes collisional and auto-ionization rates, and the recombination rate includes radiative and dielectronic recombination, which depend on temperature. For the convenience of calculation,  $C_i$  and  $R_i$  are calculated separately using precomputed tables from the CHIANTI atomic database as in Ko et al. (2010). This table lists  $C_i$  and  $R_i$  versus temperature ranging from  $10^4 \text{ K}$  to  $10^8 \text{ K}$  for most elements observed in solar atmosphere using a constant electron density of  $1.8 \times 10^8 \text{ cm}^{-3}$  because these rates are not sensitive to the electron density.

The time-dependent ionization equation is solved using the finite difference method. In order to easily integrate this solver with the other SolarSoft routines, the program is written in the IDL. The calculation starts from ionization equilibrium, and the initial ionic fraction values for each chemical element are calculated according to the equilibrium assumption. We use a second-order implicit scheme or a fourth-order explicit Runge–Kutta method to integrate Equation (1). For both numerical schemes, small time steps are necessary for computational stability. Because the temperature and the density can change by several orders of magnitude in a short time, and because the ionization rates  $C_i$  and recombination rates  $R_i$  depend strongly on the temperature,  $C_i$  and  $R_i$  can change by several orders of magnitude as well. Additional conditions are also introduced to enhance the numerical stability, including the constraint that each ionic fraction should be positive, and requiring that the total fraction for a given element be close to one, for example, by checking the accuracy threshold  $\sum f_i \geq 0.999$  at each time step and decreasing the time step if this condition is not met. The time step used to integrate Equation (1) is typically smaller than the output time interval from the MHD simulation data, so we use spline interpolation in time on the history of temperature and electron density. We have written out the MHD simulation data with a very short time step ( $0.01\tau_A$ , where  $\tau_A = 1446 \text{ s}$  is the characteristic timescale) to facilitate this procedure.

For each ion of a given element, the line emission is calculated by the following formula:

$$I_{\text{line}}(\lambda) = \frac{n_x}{4\pi n_H} \int G(T_e) dEM(T_e), \quad (2)$$

where  $I_{\text{line}}$  is in units of photon  $\text{cm}^{-2} \text{ s}^{-1} \text{ sr}^{-1}$ , and  $n_x/n_H$  is the elemental abundance based on the coronal values in the CHIANTI atomic database (Feldman et al. 1992). More recent abundances by Schmelz et al. (2012) would decrease the predicted AIA intensities by a factor of about two, but the relative differences between different AIA bands would remain unchanged.  $G$  is the contribution function that is calculated by using the ionic fraction of time-dependent ionization results and the emissivities calculated from CHIANTI (version 6), and

$dEM$  is the differential emission measure that depends on  $n_e$  and LOS length,  $dEM \propto n_e^2 L$  (e.g., Ko et al. 2010). Here we assume that the plasma is uniform along the LOS direction and set the LOS length to  $L = 10^9 \text{ cm}$ . Because  $L$  is arbitrary, only the relative line intensities or AIA count rates are meaningful. Combining with the AIA filter response, the total count rates from the emission by all elements are calculated for the AIA EUV channels as follows:

$$\text{total counts} = \sum_{\lambda} \frac{I_{\text{line}}(\lambda) \text{EA}(\lambda) E(\lambda) \Omega}{C \times G_N}. \quad (3)$$

Here the total count rates are in units of  $\text{DN s}^{-1} \text{ pixel}^{-1}$ . EA is the effective area of the filter and we obtain response curves as a function of wavelength for each AIA channel using SolarSoft routines. The spectrum is converted into energy units using  $E(\lambda) = h\nu = hc/\lambda$ .  $\Omega$  is the solid angle subtended by a pixel in the telescope, and  $C$  is a factor that converts photon energy incident on the CCD into electrons, given by

$$C = \frac{3.65 \text{ eV}}{\text{electron}} \times \frac{1.6 \times 10^{-12} \text{ erg}}{\text{eV}} \quad (4)$$

for the AIA detectors.  $G_N$  is a constant for each telescope that turns *electrons* into Data Number or DN. For AIA,  $G_N \approx 18 \text{ electrons DN}^{-1}$ .

### 3. RESULTS

In this model, the magnetic configuration initially consists of a helmet streamer embedded in a spherically symmetric solar wind solution. The system is allowed to equilibrate in the solar wind, then the magnetic configuration is evolved by imposing shearing motions at the solar surface, allowing the free magnetic energy to build up in the streamer. After that, flux cancellation is initiated at the boundary by linearly decreasing the strength of the bipolar term, which causes a formation of flux rope in the streamer. Consequently, the system loses equilibrium and erupts (see Reeves et al. 2010 for more detail).

During the eruption, a current sheet forms below the flux rope. In the initial phase, an X-point appears between the flux rope and magnetic loop near the solar surface. The current sheet is stretched, and becomes longer as the flux rope rises from the low corona. By  $360\tau_A$ , a long current sheet is created below the flux rope, which reaches a height of  $3.5 R_\odot$ .

The temperature and the plasma velocity are also high inside the current sheet due to magnetic reconnection. Figure 1 shows distributions of temperature, density, and velocity at this time ( $360\tau_A$ ). The long, thin features of the CME/flare current sheet are displayed on the temperature and density color contour maps (Figures 1(a) and (b)). The high temperature of up to  $10^7 \text{ K}$  occurs in a thin region, within about  $0.02 R_\odot$  of the symmetry axis. The density around the current sheet region is lower than ambient regions and is shown as a thin dark band on the color contour maps. This density depletion is consistent with the LASCO observations reported in Vrřnak et al. (2009). Thus density decrease happens because of the dynamic CME/flare evolution in which the magnetic reconnection inflow speed is low and the matter cannot fill in immediately due to the rapid rise of the flux rope. But in the center of the current sheet, there is a rapid increase of density. This feature is similar to previous reconnection simulations in which the density increases rapidly because of a pair of slow mode shocks (e.g., see Yokoyama & Shibata 1997). Along the current sheet, the upward magnetic

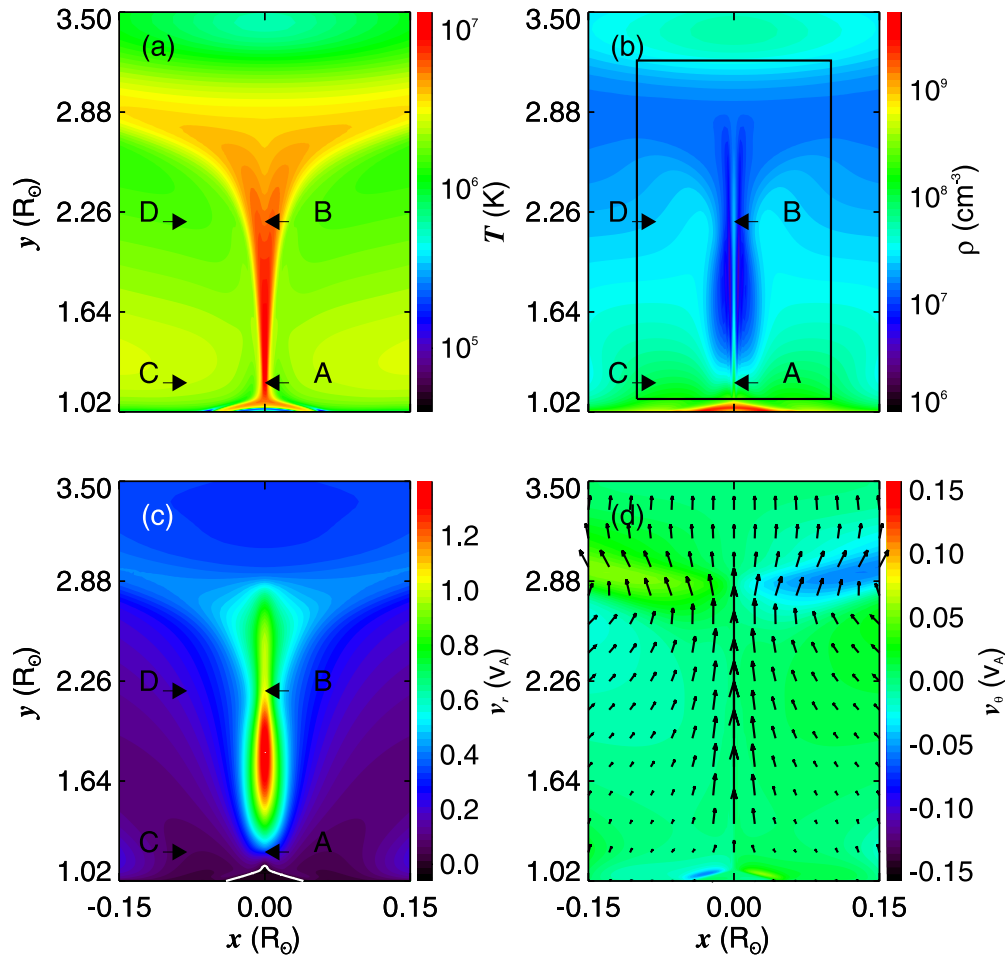


**Figure 1.** Distribution of temperature ( $T$ ), density ( $\rho$ ), and velocity ( $V_r$  and  $V_\theta$ ) at time  $360\tau_A$ . (a) Temperature: A, B, C, and D mark four sample points. (b) Density: the black rectangle is the region for ionization calculations. (c)  $V_r$ : the white line shows the profile of  $V_r = 0$ , below which  $V_r$  is less than zero. The reconnection X-point is at  $r = 1.12 R_\odot$  at this time. (d) The contour maps of  $V_\theta$ . Arrows show velocity vectors.

(A color version of this figure is available in the online journal.)

reconnection outflows are very fast and the radial component of velocity ( $V_r$ ) reaches 1.2 times the Alfvén speed ( $v_A$ ), which is higher than the other regions (Figures 1(c) and (d)). These fast flows imply that non-equilibrium ionization processes are likely to be important in the rapidly evolving system.

We examine features of ion charge states and associated emission lines at  $t = 360\tau_A$  by performing time-dependent ionization calculations. At this time, the current sheet has developed to a state with extremely high temperature and fast upward outflows. Also the current sheet is long enough so that its top extends to about  $2.5 R_\odot$  from the solar center, covering the field of view (FOV) of several space instruments, such as *SDO/AIA* and *SOHO/UVCS*. The black rectangle in Figure 1(b) shows the region from  $1.1 R_\odot$  to  $3.2 R_\odot$  with a width of  $0.2 R_\odot$  over which we consider non-equilibrium ionization effects.

### 3.1. The Ionization Properties of the Current Sheet

In this section, we calculate distributions of ionic charge states in the current sheet and surrounding regions, and show how the ionization state depends on height along the current sheet. In Figure 1(a), four sample points (A, B, C, and D) are chosen to study different positions around the current sheet at this time ( $360\tau_A$ ). Points A and B are located in the current sheet center ( $x = 0.0 R_\odot$ ), C and D are located on the ambient regions

( $x \simeq 0.08 R_\odot$ ). Points A and C have a height of  $1.2 R_\odot$ , while B and D have a height of  $r = 2.2 R_\odot$ . As Figures 1(a) and (b) show, the temperature and density are significantly different at each of these points. Inside the current sheet, the temperature is close to  $1.2 \times 10^7$  K at point A and  $5.7 \times 10^6$  K at point B. The fact that the temperature is higher on point A than on point B is partly due to adiabatic cooling from expansion. Outside the current sheet, the temperature is close to the coronal characteristic value, which is  $2.5 \times 10^6$  K for point C and  $1.6 \times 10^6$  K for point D. The ionic charge states of iron at these four points are plotted in Figure 2. The dashed lines are for equilibrium ionization, and the solid lines are for the time-dependent ionization calculations.

For the cases of equilibrium ionization, the dominant ions are Fe XXI (and Fe XVII) for points A (and B), and Fe XVII (and Fe XII) for points C (and D). The ion charge state distributions depend on the local temperature because the ionization rates and recombination rates are more sensitive to temperature than electron density under the assumption of equilibrium ionization. As the dashed lines show in Figure 2, the highest charge states of iron are found in the low end of the current sheet (point A) associated with the high temperature of  $1.2 \times 10^7$  K, but higher points in both the current sheet and the ambient region are dominated by lower charge states.

Iron charge states from our non-equilibrium ionization analysis are plotted as solid lines in Figure 2. Near the low

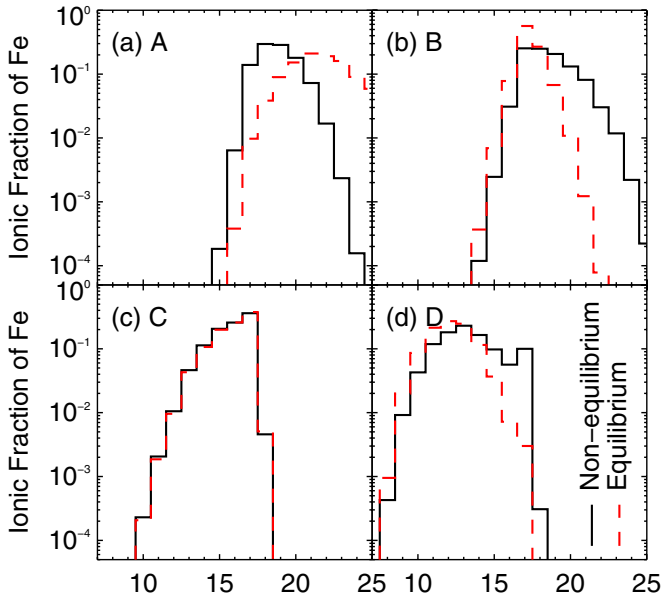


**Figure 2.** The ionic charge fraction of iron at time  $360\tau_A$  for sample points A, B, C, and D. The solid lines are for time-dependent ionization calculations and the dashed lines are for equilibrium ionization assumption. The  $x$ -axis is the charge state, which is defined as charge number ( $Q$ ) plus one (e.g., Fe XVIII is Fe of  $Q = +17$ ).

(A color version of this figure is available in the online journal.)

end of the current sheet (e.g., point A), the charge state distribution is skewed toward lower charge states compared to equilibrium ionization results. This plasma is heated from the ambient corona on timescales shorter than the ionization and recombination timescales, and thus is underionized. At the top end (point B), on the other hand, the profiles are shifted toward higher charges states. Plasma that was heated in the lower part of the current sheet cools more quickly than recombination can keep up with, and thus is overionized. The dominant ions are Fe XVIII for point A and Fe XVII for point B. Outside the current sheet, the dominant ions are Fe XVII for point C and Fe XIII for point D which is similar to the dominant ions under the equilibrium assumption.

To understand how plasma flows impact the ionic charge states for time-dependent ionization processes, we look at detailed features of magnetic reconnection flows. The trajectories of the four sample points are plotted in Figure 3(a). The flow indicates that there are three main features of the motion. First, matter flows up and moves away from the solar surface because of the solar wind outside the current sheet. It can be seen that both points C and D have moved up from the bottom. Second, downward reconnection outflow can only be seen in the low part of the current sheet and the upward reconnection outflows are dominant above the X-point (see Figure 1(c)). Because the reconnection X-point appears in the lower region of the current sheet, it is not surprising that the downward outflow is seen only in the lower part of the current sheet also (Reeves et al. 2010; Murphy 2010; Shen et al. 2011). The downward flow appears below  $r = 1.12 R_\odot$  at  $t = 360\tau_A$  and the other outflows are anti-sunward along the current sheet (see Figure 1(c)). The third flow feature is that plasma in reconnection inflow regions is also from lower heights (e.g.,  $r = 1.02 R_\odot$ ), implying that the temperature of inflow plasma can change during the motion instead of remaining at a constant characteristic coronal temperature.

Corresponding to the flow, Figure 3(b) shows how density varies with time for these four points. At the earliest time,

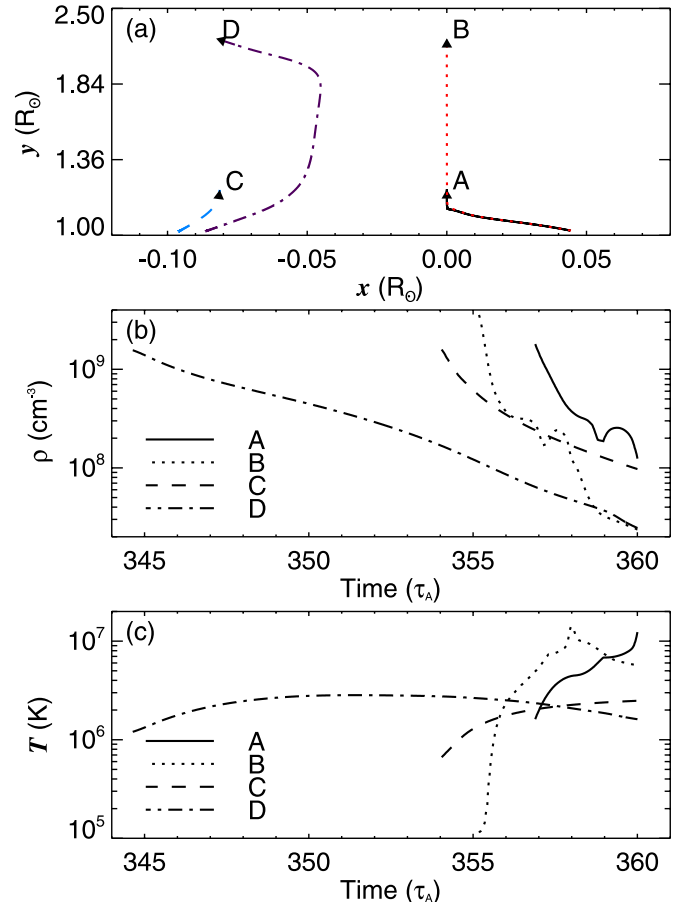


**Figure 3.** (a) Streamline for sample points A, B, C, and D, along with (b) the density history and (c) the temperature history for each of these points.

(A color version of this figure is available in the online journal.)

densities are high ( $\rho > 10^9 \text{ cm}^{-3}$ ) for all four points because they originate from roughly the same height. Then  $\rho$  decreases as the plasma moves upward. Inside the current sheet, the density at points A and B decreases rapidly from the initial value. For points C and D, changes in density are more gradual.

As Figure 3(c) shows, the temperature histories differ significantly among these sample points. For point A, the temperature rapidly increases to more than  $10^7 \text{ K}$  until the final time ( $360\tau_A$ ). Point B is first heated up to more than  $1.4 \times 10^7 \text{ K}$  at time  $358\tau_A$ , and then drops to  $5.7 \times 10^6 \text{ K}$  at  $360\tau_A$ . Outside the current sheet, points C and D have lower maximum temperatures and they change more gradually than the points inside the current sheet. The different temperature histories depend on the proximity to the reconnection diffusion region. The extremely high temperature ( $> 10^7 \text{ K}$ ) results from ohmic heating, which efficiently converts the magnetic energy into heat in high current density regions such as the current sheet. Because thermal conduction is included in this MHD model, high temperatures can also be found over a large range of heights along the current sheet where the current density is not very high but the thermal conduction is efficient. On the outside regions of the current sheet, there is little ohmic heating. The heat conduction causes a thin high temperature region surrounding the current sheet (e.g., see also Yokoyama & Shibata 1997; Seaton & Forbes 2009). As the plasma moves close to the reconnection diffusion region, it is heated to extremely high temperatures. According to streamlines, point A is not close to the diffusion region until time  $360\tau_A$ , but point B crosses the diffusion region that is

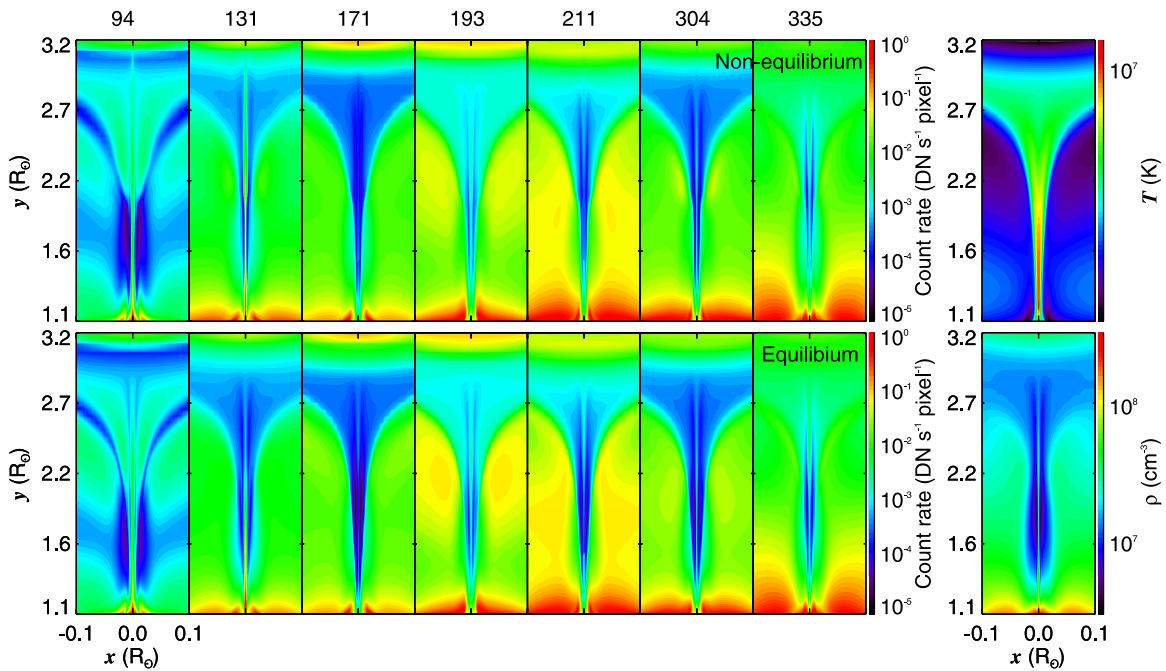


**Figure 4.** Predicted *SDO/AIA* count rates in the local region around the current sheet at time  $360\tau_A$ . The top panels are for time-dependent ionization results and the lower panels are for equilibrium assumption. The right two panels show that the distribution of temperature and density at the same time. All color bars are logarithmic scales.

(A color version of this figure is available in the online journal.)

located on the roughly same height at earlier times. This behavior explains the early increase to  $1.4 \times 10^7$  K in the temperature history of point B. Points C and D perform similar motions; they move slowly and are close to the outside regions of the magnetic diffusion region instead of crossing through it. Their temperatures stay low and change slowly.

The features of the reconnection inflow and outflow affect the properties of the ionization processes. At low altitude within the current sheet, the ionic charge states correspond to lower temperatures because the plasma started out relatively cool and was heated rapidly. On the other hand, the top end of the current sheet shows high temperature ionization features although it is now located at a lower temperature. Outside the current sheet, the ionization states are also affected by temperature history which changes slowly, but they are close to equilibrium in the low corona region due to the high electron density there.

Compared with the similar calculations using the same CME flux-cancellation model reported by Lynch et al. (2011), this work focuses on the current sheet region below the erupting flux rope. The time considered in this work is also earlier,  $32\tau_A$ , than their calculations because we look at this special time when most of the current sheet could be covered by the FOV of several UV (and EUV) observational instrument. In the upper part of the current sheet, the overionized charge states are similar to the calculation according to the same CME flux-cancellation model reported by Lynch et al. (2011) in which the reconnection outflow jets encounter the flux rope and cause thermal ionization features. However, our calculations show that the higher temperature and higher outflow speed inside the current sheet cause the ionization properties to be significantly different from the flux rope regions. For instance, the current sheet has higher ionization features than other regions and the ion charge states of iron are dominated by Fe XVI and higher ionized states. We also note that the ionization “freezing-in” height is roughly  $2 R_\odot$  in our calculations for the current sheet, which is different from

the height of  $2 \sim 3 R_\odot$  according to Rakowski et al. (2007), and is from the heights of  $\sim 6 R_\odot$  and  $1.5 \sim 2 R_\odot$  for CME flux-cancellation and magnetic breakout CME models reported by Lynch et al. (2011). The freezing-in heights vary with time and position, since they depend on the different histories of temperature and electron density dropping with height and also on the different flow speed among these models.

### 3.2. Predicted AIA Images

To get the predicted *SDO/AIA* images for this CME/flare model, we make the above time-dependent ionization calculations for the elements which contribute significantly to coronal emission, including He, C, N, O, Ne, Mg, Al, Si, S, Ar, Ca, Fe, and Ni. For each element, the emission line intensities are calculated and then the *SDO/AIA* effective areas are applied to get emission in each wave band. Finally, the total intensities of all emission lines from these elements are calculated at each pixel around the current sheet on the 2D plane. We did not degrade the resolution to match AIA images.

Figure 4 shows predicted AIA count rate images from the simulation data. The first row shows intensities for time-dependent ionization calculations and the second row shows intensities for the equilibrium ionization results, respectively. An overall feature is that the count rates of the current sheet are either higher or lower than the ambient regions in different AIA channels. For AIA 94 Å and AIA 131 Å, bright thin regions exist in which the emissions are stronger than in ambient regions. For the other AIA channels, the intensities are weaker along the current sheet. Compared with the equilibrium assumption, the intensity of the current sheet center is significantly different in the non-equilibrium result and the bright thin current sheet region extends higher in the AIA 94 Å and 131 Å channels. In regions surrounding the current sheet, the distribution of intensity is similar for the two ionization calculations. Because the difference between the two ionization calculations depends

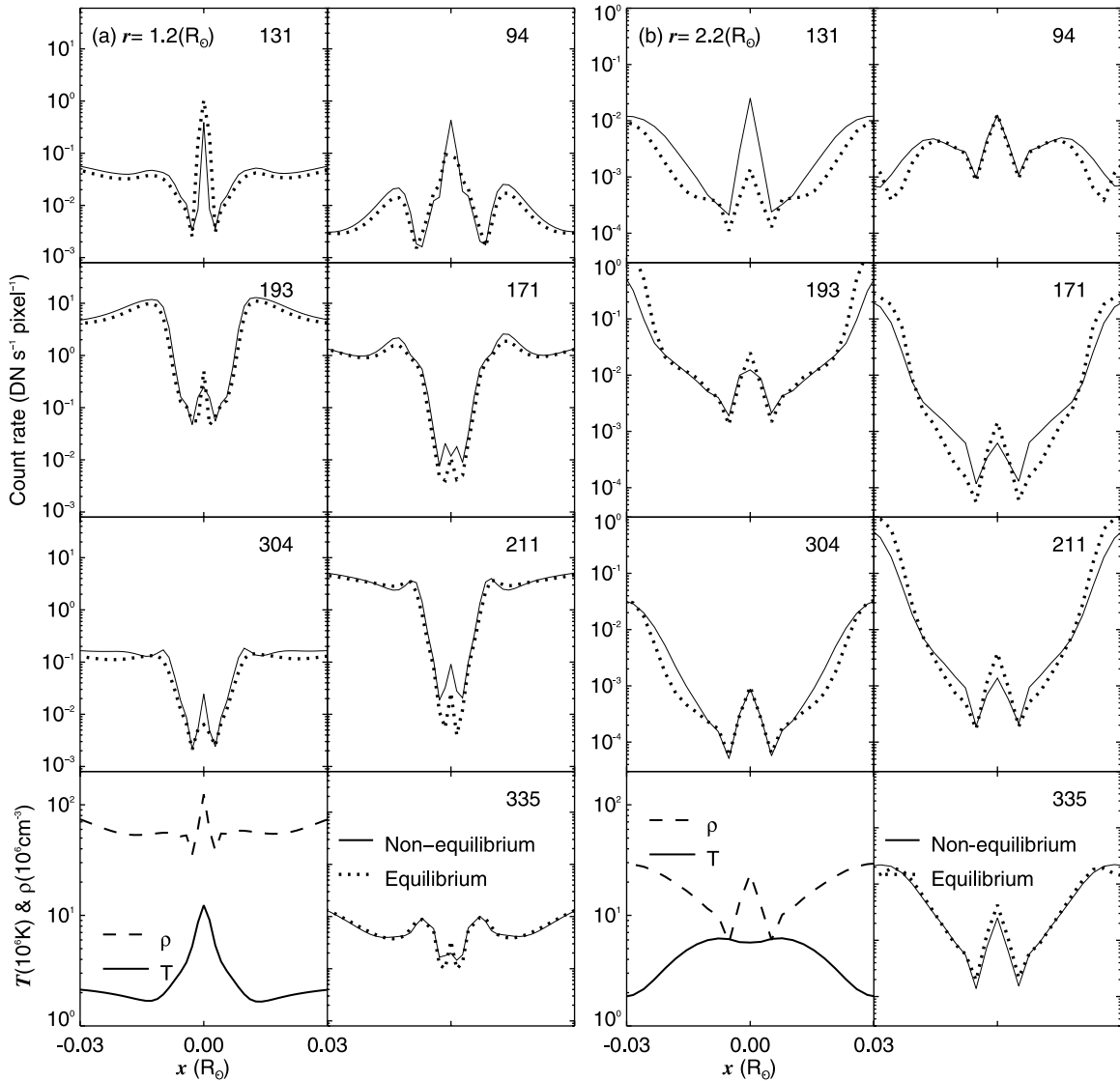


**Figure 5.** The profiles of AIA count rates at different heights:  $r = 1.2 R_{\odot}$  (a) and  $r = 2.2 R_{\odot}$  (b). The center of the current sheet is located at  $x = 0$ . The solid lines are for time-dependent ionization results and the dotted lines are for equilibrium ionization. The profiles of temperature (solid lines) and density (dashed lines) are shown on the lower right panel.

on height, we look at the distribution of intensity at different heights along the current sheet in the following parts.

Figure 5 plots the distributions of count rates along the  $x$ -direction across the current sheet for two different heights,  $r = 1.2 R_{\odot}$  and  $r = 2.2 R_{\odot}$ . The solid line is for non-equilibrium ionization calculations and the dotted line is for equilibrium assumption. While the height of  $2.2 R_{\odot}$  is outside the AIA FOV, this analysis is appropriate for guiding the development of future instrumentation. The count rates reach the maximum at the center of the current sheet ( $x = 0$ ) for AIA 94 Å and 131 Å channels because of the high temperatures there. However, for other AIA bands, the count rates in the current sheet center are lower than the background plasma, for example, the count rate of AIA 193 Å is less than  $0.5 \text{ (DN s}^{-1} \text{ pixel}^{-1})$  in the center of the current sheet but it close to  $10 \text{ (DN s}^{-1} \text{ pixel}^{-1})$  outside the current sheet at  $r = 1.2 R_{\odot}$ . Despite this, a local maximum in intensity appears in the center of current sheet for AIA 171 Å, 193 Å, 211 Å, 304 Å, and 335 Å. Compared to the distributions of density and temperature shown in Figure 5, it is clear that the peak structures in AIA 171–335 Å do not

correspond to either density or temperature profiles. Around the current sheet, low-intensity regions surround the current sheet in the AIA 94 Å and 131 Å channels. We shall discuss this in the next paragraph.

Along the current sheet ( $y$ -direction), the dependence of count rates of the AIA bands on height is shown in Figure 6 for both time-dependent and equilibrium ionization calculations. The intensities decrease with height along the current sheet at first for all the channels, and then increase again near the bottom of CME flux rope. This tendency is associated with the density profile that shows the density of the current sheet is higher in the low corona, while at the top end of the current sheet, the density becomes high again because the outflow encounters the CME flux rope. The emission profiles with height are different from the profile of temperature shown in Figure 6(c) along the current sheet. On the top end, the temperature has decreased to  $1.6 \times 10^6 \text{ K}$  and the density also becomes low, but the intensities of AIA 94 Å and AIA 131 Å channels appear higher than equilibrium ionization assumption because of time-dependent ionization.

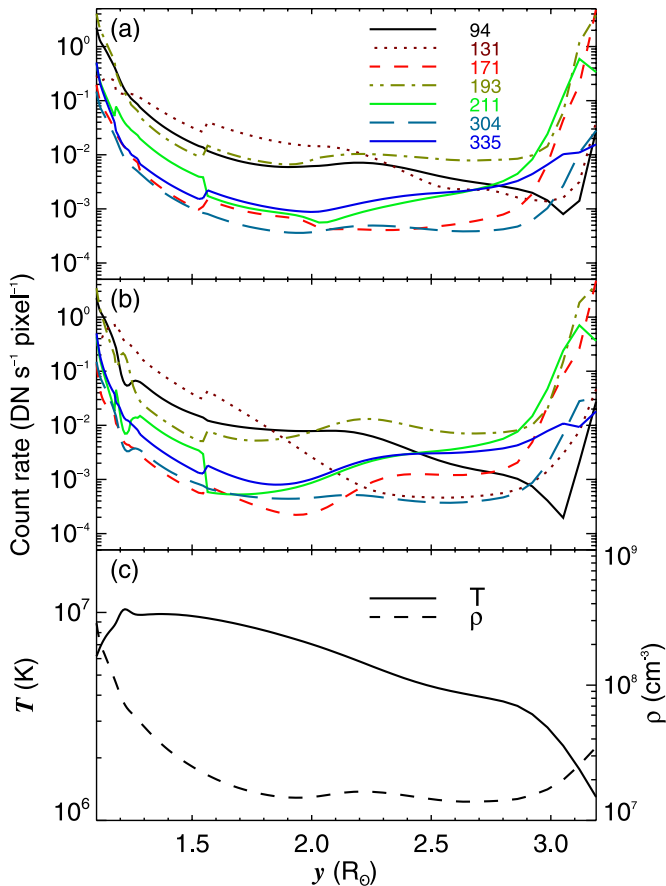


**Figure 6.** Variation of predicted SDO/AIA count rates as a function of height along the current sheet. Time-dependent ionization results are plotted in (a) and equilibrium ionization results are shown in (b). The temperature (solid lines) and density distribution (dashed lines) are shown in (c).

(A color version of this figure is available in the online journal.)

To study where the time-dependent ionization strongly affects the emission along the current sheet, we calculated the relative difference of emission between time-dependent calculations and equilibrium ionization assumption by defining  $I_\delta$  as

$$I_\delta = (I_{\text{non}} - I_{\text{ei}})/(I_{\text{non}} + I_{\text{ei}}), \quad (5)$$

where  $I$  is the average in a small regular region covering five grid points along the center of the current sheet.  $I_{\text{non}}$  is the emission intensity for time-dependent ionization calculations, and the  $I_{\text{ei}}$  is for equilibrium ionization results, respectively. The relative difference  $I_\delta$  indicates the degree that ionization process deviates from the equilibrium ionization assumption.

Figure 7(a) shows how  $I_\delta$  varies with height along the current sheet.  $I_\delta$  displays different characteristics in the low part and the high part of the current sheet. In the low part ( $r < 2.0 R_\odot$ ),  $I_\delta$  is negative for AIA 94 Å and AIA 131 Å channels, while it is larger than zero for other channels. Even though the temperatures in the low part of the current sheet are high (shown in Figure 6(c)), intensities in the high-temperature emission lines (AIA 94 Å and AIA 131 Å) predicted by non-equilibrium ionization are weak compared to equilibrium. In the high part along the current sheet ( $r > 2.2 R_\odot$ ), the tendencies are reversed.  $I_\delta$  for AIA 94 Å and AIA 131 Å channels are positive in most regions except the bottom of the CME flux rope where the density is high.

The variation of  $I_\delta$  outside the current sheet versus height is plotted in Figure 7(b). Here we show that  $I_\delta$  along the

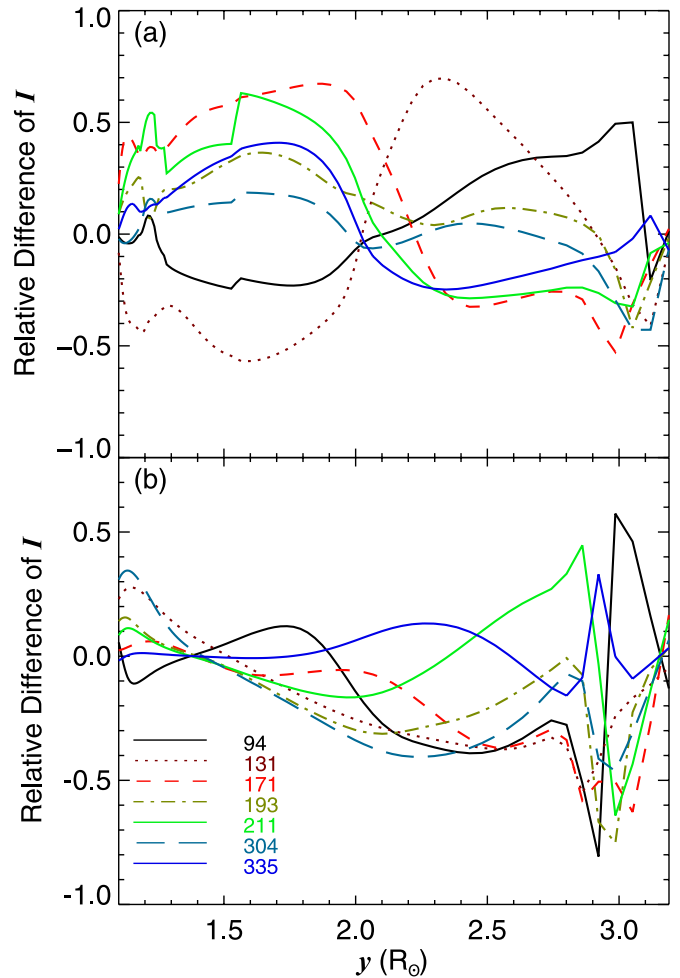


**Figure 7.** Variation of  $I_\delta$  as a function of height. Here the  $I_\delta = (I_{\text{non}} - I_{\text{ei}})/(I_{\text{non}} + I_{\text{ei}})$  is the relative difference of predicted SDO/AIA count rate between non-equilibrium and equilibrium ionization calculations. (a) Along the current sheet. (b) On the direction of polar angle  $\theta = 1.48$ .

(A color version of this figure is available in the online journal.)

radial direction outside the current sheet, at the polar angle  $\theta = 1.48$  radians defined from the Sun center. An obvious feature of these curves is that the absolute value of  $I_\delta$  tends to increase with height. For AIA 94 Å and AIA 131 Å, the absolute values of  $I_\delta$  is low, between 0.12 and 0.28 in the low part of current sheet, but increase to 0.81 and 0.55 in the high regions. This means that the difference of the time-dependent ionization from equilibrium ionization assumption becomes significant in high regions.

According to the curves shown in Figure 7, time-dependent ionization strongly affects the AIA emission for both low and high heights along the CME/flare current sheet. Compared with the equilibrium ionization assumption, in the lower part of current sheet, the intensities are smaller for AIA 94 Å and 131 Å but larger for other AIA channels. In the higher part of current sheet, the case is reversed in that the temperature has already decreased below  $10^7$  K, but the ions stay at higher charge states as shown in Figure 2(b). In ambient regions, the equilibrium assumption is not appropriate at higher altitude. Because the density decreases with height, non-equilibrium process becomes important in this region.

These conditions occur because the heating occurs at low heights, and the ionization state lags behind the temperature increase. However, the plasma cools as it moves up along the

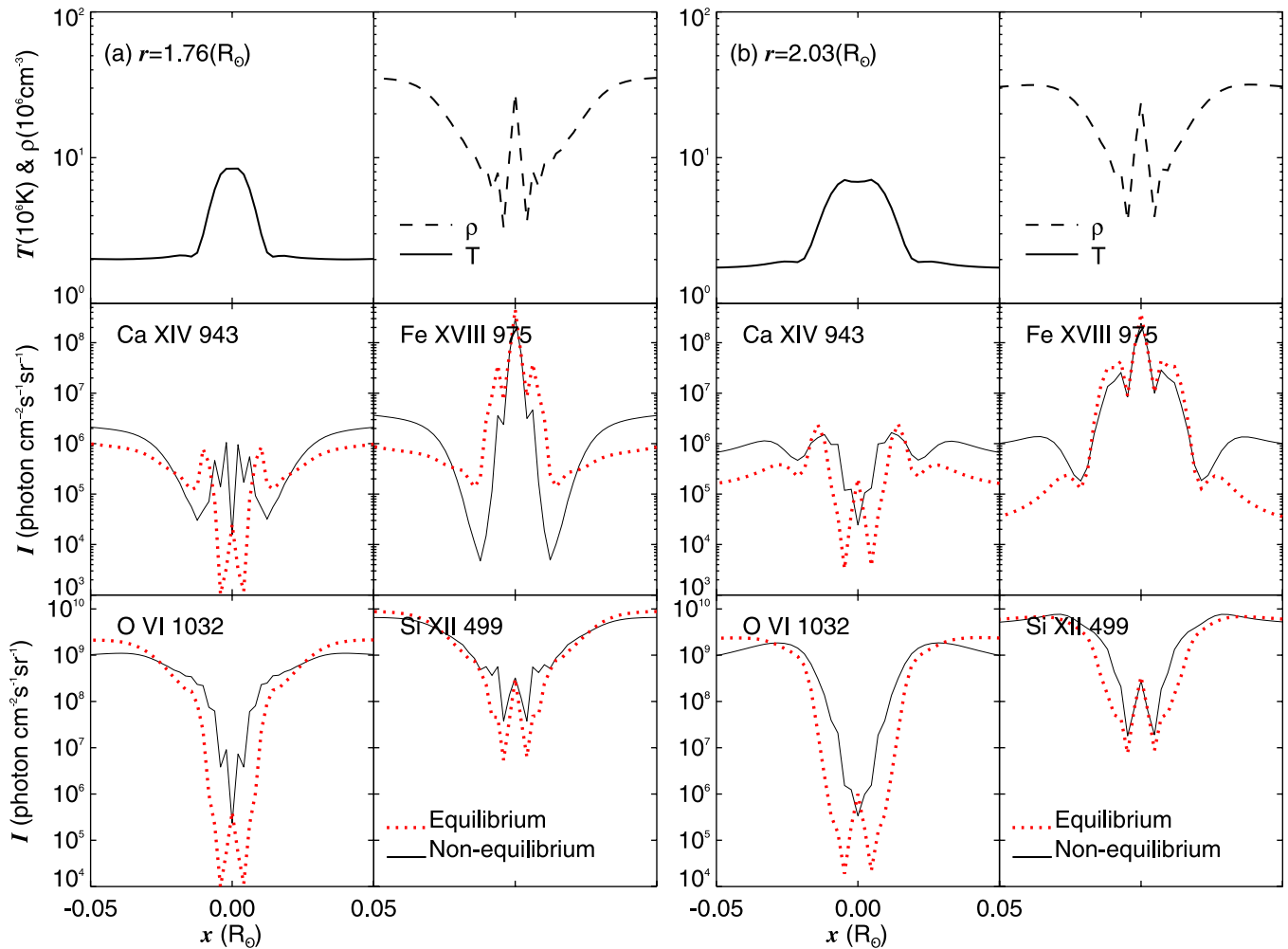


**Figure 8.** The predicted intensities of UV emission lines of [Fe XVIII]  $\lambda$ 975, [Ca XIV]  $\lambda$ 943, Si XII  $\lambda$ 499, and O VI  $\lambda$ 1032 in the direction across the current sheet at heights of  $1.76 R_{\odot}$  (a) and  $2.03 R_{\odot}$  (b). The solid lines are for time-dependent ionization results and the dotted lines are for equilibrium assumption. The temperature and density are plotted in the top panels.

(A color version of this figure is available in the online journal.)

current sheet, and the recombination cannot keep up with the temperature drop. At about  $2 R_{\odot}$  the declining temperature is roughly equal to temperature corresponding to the ionization state in equilibrium.

### 3.3. Predicted UV Images

We compute the intensities of [Fe XVIII]  $\lambda$ 975, [Ca XIV]  $\lambda$ 943, Si XII  $\lambda$ 499, and O VI  $\lambda$ 1032, which are reported in observational studies of CME/flare current sheets using *SOHO*/UVCS (Kohl et al. 1995, 1997). Following the time-dependent ionization calculations, we plot the profiles across the current sheet of these UV emission lines at heights  $r = 1.76 R_{\odot}$  and  $r = 2.03 R_{\odot}$  in Figure 8. Here the  $1.76 R_{\odot}$  and  $2.03 R_{\odot}$  are typical heights for UVCS observations. As a comparison, we also plotted a dotted line indicating predicted emission intensities in equilibrium ionization.

In the  $x$ -direction across the current sheet, the intensity at the center is either enhanced or depressed relative to the ambient region. Figure 8(a) shows an extremely high intensity peak that is located in the center of the current sheet for [Fe XVIII]  $\lambda$ 975. On the other hand, for [Ca XIV]  $\lambda$ 943, Si XII  $\lambda$ 499, and O VI  $\lambda$ 1032, there is a weak peak appearing in the current sheet center but with intensities that are lower than the ambient intensities. Figure 8(b) shows similar profiles at height  $r = 2.03 R_{\odot}$ . The

intensity of the peak for [Fe XVIII]  $\lambda$ 975 has a similar value as the case  $r = 1.76 R_{\odot}$  but the width is larger due to the extended current sheet.

Another feature of these emission lines is that a low-intensity region surrounds the current sheet. For [Fe XVIII]  $\lambda$ 975, the minimum intensities ( $I \simeq 5 \times 10^{-4}$  photons  $\text{cm}^{-2} \text{s}^{-1} \text{sr}^{-1}$ ) exist in the current sheet boundary regions ( $x = \pm 0.02 R_{\odot}$ ) in Figure 8(a), and appear as a thin sheath around the current sheet. These features are also mentioned in the previous sections in which the dark sheath is seen around the bright center of the current sheet (Figure 5). Furthermore, the low-intensity region is found in a large range from the low end of the current sheet to the higher altitude  $r = 2.2 R_{\odot}$ .

According to profiles of the intensities of these UV lines and distributions of  $T$  and  $\rho$  shown in Figure 8, it is clear that the low-intensity region does not indicate low temperature. Because the emission line intensity is proportional to the square of density according to the above assumption, the sheath is affected by the low-density regions though the profiles of the sheath do not simply correspond to density profiles in  $x$ -direction. The sheath is deeper in the non-equilibrium results than the equilibrium ionization calculation. This indicates that the low-intensity sheath feature can be enhanced by the time-dependent ionization process.

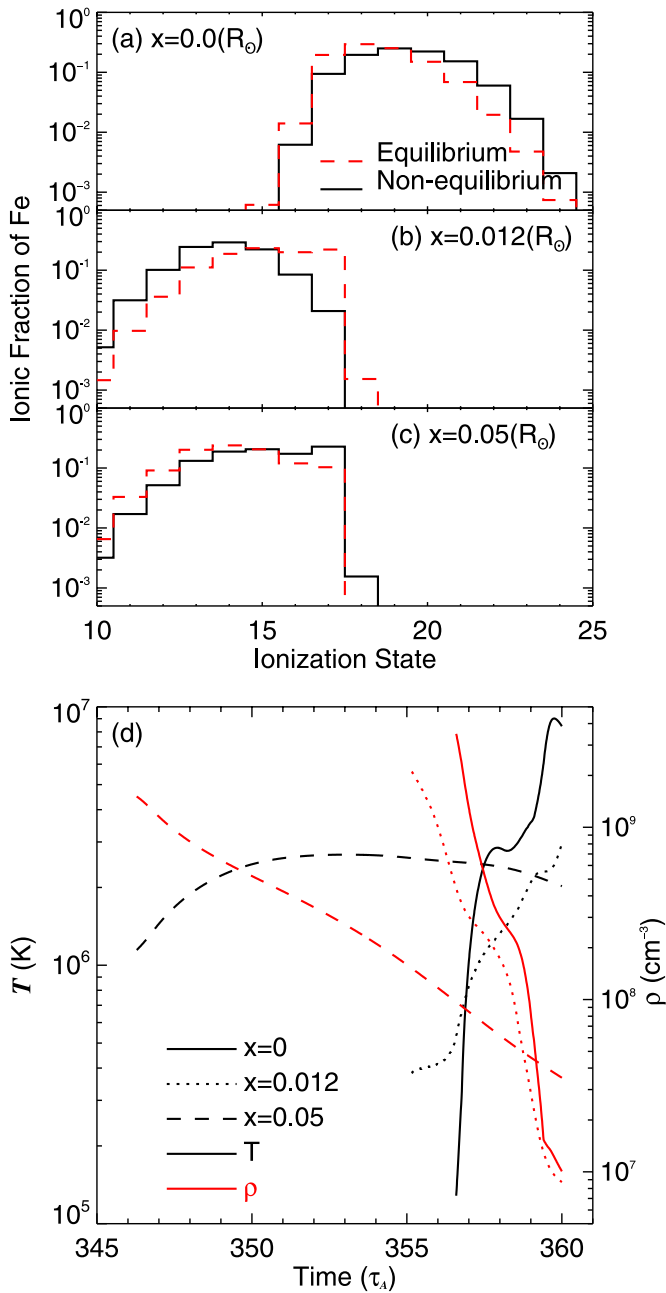


**Figure 9.** (a), (b), and (c) shows the ionization states of iron for three sample points around the sheath region, which are located on  $x = 0.0, 0.012,$  and  $0.05$  at the height of  $1.76 R_{\odot}$ . The temperature and density history corresponding to these points are plotted in (d), where black lines are for temperature and red lines are for density.

(A color version of this figure is available in the online journal.)

We also notice that the intensity of  $[\text{Ca XIV}] \lambda 943$  and  $\text{O VI} \lambda 1032$  at the current sheet center for the non-equilibrium case is a “dip” while it is a peak for the equilibrium case. The latter is an obvious reflection of both the electron density and temperature profiles. This shows that the effect of non-equilibrium ionization is a dominating factor for  $[\text{Ca XIV}] \lambda 943$  and  $\text{O VI} \lambda 1032$ . On the other hand,  $[\text{Fe XVII}] \lambda 975$  and  $\text{Si XII} \lambda 499$  results show that the density peak at the current sheet center still plays a crucial role in determining the intensity profile across the current sheet in either case.

To discuss how non-equilibrium ionization could cause the deep sheath in UV line profiles, Figure 9 shows the charge state

of iron around the sheath region at a height of  $1.76 R_{\odot}$  and plots the evolution history of the temperature and density of three sample points in this height. Figures 9(a), (b), and (c) are in the order of  $0.0, 0.012,$  and  $0.05 R_{\odot}$ , which are located in the ambient region, the sheath region, and the center of the current sheet, respectively. In the sheath region ( $x = 0.012 R_{\odot}$ ), ionic charge states are dominated by the lower ionized ions compared to equilibrium ionization (see Figure 9(b)). Because the temperature increases rapidly from  $10^6$  K to around  $3 \times 10^6$  K in a short period, the time-dependent ionization strongly affects the charge state profiles and causes the appearance of lower temperature ( $< 3 \times 10^6$  K) ionization features. On the other hand, Figure 9(d) shows that the density  $\rho$  in the sheath region also decreases to a minimum value ( $9 \times 10^6 \text{ cm}^{-3}$ ) that is less than both the current sheet center ( $10^7 \text{ cm}^{-3}$ ) and the ambient region ( $3.4 \times 10^7 \text{ cm}^{-3}$ ). This decrease causes the intensity of the sheath to be lower than ambient regions. As a result, the low-intensity region becomes deep in the time-dependent ionization calculations. A similar low-temperature sheath has been observed in the 2003 November 4 event observed by UVCS (Ciaravella & Raymond 2008). A detailed comparison with observational data needs further study because our current computations assume a symmetric structure and do not contain projection effects or non-uniform plasma environments.

#### 4. CONCLUSION

Using the global CME/flare model analyzed by Reeves et al. (2010), we calculate the time-dependent ionization state using the numerical simulation data, and we predict the UV emission line intensities and the count rates in *SDO/AIA* bands. These predicted intensities of AIA bands are relevant for new UV instruments such as the Interface Region Imaging Spectrograph (IRIS), where the AIA 193 Å band will be similar to IRIS Fe XII and the AIA 131 Å band will be similar to IRIS Fe XXI. The predicted 2D intensity images for AIA bands are obtained for this eruption model. The distributions of predicted intensities depend on the temperature, density, and reconnection outflow speed. The features of the emission line intensities around the CME/flare current sheet are studied and summarized.

1. The difference between equilibrium ionization and non-equilibrium ionization will cause temperatures to be underestimated at low heights and overestimated at large heights by about a factor of two if equilibrium is assumed in interpreting the data.
2. The predicted 2D intensity images for AIA bands are computed for this model. For AIA 94 Å and 131 Å channels, the center of the current sheet appears as a bright feature where the count rates are higher than in the ambient regions. On the other hand, the current sheet shows weak intensities compared with the ambient regions for other AIA channels. Time-dependent ionization results show that the bright current sheet extends to a higher height for AIA 94 Å and 131 Å channels compared to the equilibrium case.
3. The impact of time-dependent ionization on the count rates of *SDO/AIA* bands is significant along the current sheet. Compared with equilibrium ionization, there is a large relative difference ( $I_s$ ) in AIA count rates from the top of the post-flare loops to the bottom of the erupting CME flux rope. This result implies that non-equilibrium ionization needs to be calculated even at low heights because the ionization and recombination timescales may exceed the transit time of the high-speed reconnection outflow.

4. According to the intensity distributions in the simulated AIA images, there are two interesting regions in the current sheet as a function of height. In the low part of the current sheet, the intensities of AIA 94 Å and 131 Å channels are lower in the case where non-equilibrium ionization is assumed, compared to the equilibrium case.  $I_\delta$  is negative in this part of the current sheet. In the high part of the current sheet, the intensities of AIA 94 Å and 131 Å channels for the assumption of time-dependent ionization are higher than the predicted value for the equilibrium case and  $I_\delta$  has a positive value. The other AIA channels show the opposite trend with height. A dividing point of these two parts along the current sheet is located around  $r = 2.1 R_\odot$  at time  $360\tau_A$ , and the detailed motion of this dividing point need more study in the future.
5. In the ambient regions outside the current sheet, the impact of time-dependent ionization on the emission line increases with height. In this region, the velocity of plasma flow is stable and slow so non-equilibrium ionization is only important in the high corona where the electron density is small. For example, the relative intensity in differences ( $I_\delta$ ) for AIA bands between time-dependent ionization and equilibrium assumption are  $\lesssim 35\%$  below at the height  $r = 2.0 R_\odot$ .
6. In the direction across the current sheet, we also computed the emission line intensities for several *SOHO*/UVCS lines according to the time-dependent ionization calculations. Low-intensity regions around the current sheet are found in several UV emission lines ([Fe xviii]  $\lambda 975$  and [Ca xiv]  $\lambda 943$ ) and *SDO*/AIA bands for the time-dependent ionization. These low-intensity regions are the result of both time-dependent ionization and distributions of  $T$  and  $\rho$  along the direction across the current sheet. For the equilibrium ionization case, the low-intensity region is caused by the lower density structure. When time-dependent ionization processes are considered, the low-intensity region becomes deeper because the lower ionization features appear in these regions. These low-intensity regions could be compared to observations. We also note that observational data depend on both the projection effects and the plasma environment. The comparison between observational data and predicted intensities needs more study.
7. Inside the current sheet, the [Fe xviii]  $\lambda 975$  profile shows that the maximum peak is located in the center of current sheet, while the [Ca xiv]  $\lambda 943$ , Si xii  $\lambda 499$ , and O vi  $\lambda 1032$  profiles are less bright at the current sheet center. The individual lines depend strongly on the details of the particular current sheet.

The authors appreciate the referee for valuable comments and suggestions that helped improve this paper. This research was supported by NASA grant NNX11AB61G, NNX11AQ13I and NSF SHINE grant AGS-1156076 to the Smithsonian Astrophysical Observatory. This work was also supported by Program 973 grants 2011CB811403 and 2013CBA01503, NSFC grant 11273055, and CAS grant KJCX2-EW-T07 to the Yunnan Astronomical Observatory. J.A.L. and Z.M. were supported by NASA (Heliophysics theory program) and NSF (Frontiers in Earth System Dynamics).

## REFERENCES

- Akmal, A., Raymond, J. C., Vourlidas, A., et al. 2001, *ApJ*, **553**, 922  
 Bemporad, A., Poletto, G., Suess, S. T., et al. 2006, *ApJ*, **638**, 1110  
 Carmichael, H. 1964, in *The Physics of Solar Flares*, ed. W. N. Hess (NASA Special Publication, Vol. 50; Washington, DC: NASA), 451  
 Ciaravella, A., & Raymond, J. C. 2008, *ApJ*, **686**, 1372  
 Ciaravella, A., Raymond, J. C., Li, J., et al. 2002, *ApJ*, **575**, 1116  
 Ciaravella, A., Webb, D. F., Giordano, S., & Raymond, J. C. 2013, *ApJ*, **766**, 65  
 Feldman, U., Mandelbaum, P., Seely, J. L., et al. 1992, *ApJS*, **81**, 387  
 Gruesbeck, J. R., Lepri, S. T., & Zurbuchen, T. H. 2012, *ApJ*, **760**, 141  
 Gruesbeck, J. R., Lepri, S. T., Zurbuchen, T. H., et al. 2011, *ApJ*, **730**, 103  
 Hirayama, T. 1974, *SoPh*, **34**, 323  
 Imada, S., Murakami, I., Watanabe, T., et al. 2011, *ApJ*, **742**, 70  
 Ko, Y.-K., Raymond, J. C., Lin, J., et al. 2003, *ApJ*, **594**, 1068  
 Ko, Y.-K., Raymond, J. C., Vršnak, B., et al. 2010, *ApJ*, **722**, 625  
 Kohl, J. L., Esser, R., Gardner, L. D., et al. 1995, *SoPh*, **162**, 313  
 Kohl, J. L., Noci, G., Antonucci, E., et al. 1997, *SoPh*, **175**, 613  
 Kohl, J., Noci, G., Cranmer, S., & Raymond, J. 2006, *A&ARv*, **13**, 31  
 Kopp, R. A., & Pneuman, G. W. 1976, *SoPh*, **50**, 85  
 Landi, E., Raymond, J. C., Miralles, M. P., et al. 2010, *ApJ*, **711**, 75  
 Landi, E., Raymond, J. C., Miralles, M. P., et al. 2012, *ApJ*, **751**, 21  
 Lin, J., & Forbes, T. G. 2000, *JGR*, **105**, 2375  
 Lin, J., Raymond, J. C., & van Ballegoijen, A. A. 2004, *ApJ*, **602**, 422  
 Lin, J., Ko, Y.-K., Sui, L., et al. 2005, *ApJ*, **622**, 1251  
 Lin, J., & Soon, W. 2004, *NewA*, **9**, 611  
 Lynch, B. J., Reinard, A. A., Mulligan, T., et al. 2011, *ApJ*, **740**, 112  
 Martens, P. C. H., & Kuin, N. P. M. 1989, *SoPh*, **122**, 263  
 Murphy, N. A. 2010, *PhPI*, **17**, 112310  
 Murphy, N. A., Raymond, J. C., & Korreck, K. E. 2011, *ApJ*, **735**, 17  
 Rakowski, C. E., Laming, J. M., & Lyutikov, M. 2011, *ApJ*, **730**, 30R  
 Rakowski, C. E., Laming, J. M., & Susan, T. L. 2007, *ApJ*, **667**, 602  
 Raymond, J. C., Ciaravella, A., Dobrzycka, D., et al. 2003, *ApJ*, **597**, 1106  
 Reeves, K. K., & Golub, L. 2011, *ApJL*, **727**, L52  
 Reeves, K. K., Linker, J. A., Mikić, Z., et al. 2010, *ApJ*, **721**, 1547  
 Reinard, A. A., Lynch, B. J., & Mulligan, T. 2012, *ApJ*, **761**, 175  
 Savage, S. L., McKenzie, D. E., Reeves, K. K., et al. 2010, *ApJ*, **722**, 329  
 Schmelz, J. T., Reames, D. V., Steiger, R. V., et al. 2012, *ApJ*, **755**, 33  
 Seaton, D. B., & Forbes, T. G. 2009, *ApJ*, **701**, 348  
 Shen, C., Lin, J., & Murphy, N. A. 2011, *ApJ*, **737**, 14  
 Sturrock, P. A. 1968, in *IAU Symp. 35, Structure and Development of Solar Active Regions*, ed. K. O. Kiepenheuer (Dordrecht: Reidel), 471  
 Vršnak, B., et al. 2009, *A&A*, **499**, 905  
 Weber, W. J., Boris, J. P., & Gardner, J. H. 1979, *CoPhC*, **16**, 243  
 Yokoyama, T., & Shibata, K. 1997, *ApJL*, **474**, L61